Hindawi
Advances in Civil Engineering
Volume 2021, Article ID 6674239, 18 pages
https://doi.org/10.1155/2021/6674239

Research Article

Compressive Capacity of Vortex-Compression Nodular Piles

Chunbao Li,[1] **Xiaosong Ma**,[1] **Shifeng Xue**,[1] **Haiyang Chen**,[1] **Pengju Qin**,[2] **and Gaojie Li**[1]

[1]*Department of Civil Engineering, China University of Petroleum (East China), Qingdao 266580, China*
[2]*College of Civil Engineering, Taiyuan University of Technology, Taiyuan 030024, China*

Correspondence should be addressed to Chunbao Li; 20070048@upc.edu.cn

Received 4 November 2020; Revised 25 December 2020; Accepted 30 December 2020; Published 13 January 2021

Academic Editor: Xinyu Ye

Compared with traditional equal-section pile, the nodular parts of nodular pile expand the contact area between the pile and foundation soil, which can greatly improve the bearing capacity of pile foundation and increase the stability of pile body structure. In this paper, the mechanism of pile-soil interaction in the construction of vortex-compression nodular pile is studied with the purpose of evaluating the compressive capacity of nodular piles. Through the indoor model test and ABAQUS numerical simulation analysis, the compressive characteristics of 12 types of vortex-compression nodular pile are obtained, and the variation rules of the parameters of the compressive characteristics of vortex-compression nodular piles are quantitatively analyzed, including the failure pattern of foundation soil, load-settlement relationship, and load transfer law of vortex-compression nodular piles. The results showed that the compressive capacity of vortex-compression nodular piles has significant advantages over that of traditional equal-section piles. Based on the results of the indoor model test and numerical simulation, the calculation method and formula of the compressive capacity of vortex-compression nodular piles are given by modifying the corresponding calculation formula of traditional nodular piles. The new method and formula are more in line with the actual working conditions and provide theoretical and data support for the further engineering application of vortex-compression nodular piles.

1. Introduction

In recent years, the number of infrastructures such as large buildings, long-span bridges, highways and high-speed railways, large oil and gas storage tanks, and offshore platforms has increased rapidly, and all of above need to be built on a specific geological condition, which puts forward higher requirements for the design and application of pile foundation. During the initial design and later construction of pile foundation, engineers and technicians have found that the failure of the pile foundation structure is mainly caused by the destruction of foundation soil, and the role of the pile body does not fully play even though the bearing capacity of the pile itself is large. Under this background, engineers have put forward the structure form of nodular piles [1, 2], which can expand the contact area between pile and soil by setting nodular parts at different positions on the pile body so as to obtain the larger bearing capacity of single pile and reduce the project cost. Nodular pile has been preferred option duo to its convenient construction and superior performance. In the near future, it may replace the traditional bored pile [3–5] and play a leading role in pile foundation engineering.

Until now, many kinds of nodular piles have been developed. Their pile formation mechanism, bearing characteristics, load transfer theory, and bearing capacity calculation method are different. Hill [6] proposed the spherical cavity expansion theory and derived the general solution of the relation between the reaming displacement and the reaming force of Tresca material. Houlsby and Yu [7] adopted the More–Coulomb yield criterion of the uncorrelated flow method and used the dilation angle to describe the soil's dilatation characteristics. They considered the large deformation in the plastic region and thus adopted the logarithmic strain to analyze the pore expansion of the ideal perfect elastic-plastic material and obtained the unified analytical solution for the pore expansion of the spherical and cylindrical cavity under the condition of unlimited deformation. Cui [8] carried out static load tests and obtained the influence law of the disc spacing on the ultimate

bearing capacity of the pile. Hu et al. [9] analyzed the mechanism and reasons for the increase in bearing capacity of branch and disc pile and modified the ultimate bearing capacity of branch and disc pile with expanded part based on the ultimate bearing capacity of straight pole pile. Zhou et al. [10] used ANSYS finite element software to study the vertical load transfer mechanism of expanded branch pile under the change of physical and mechanical parameters of soil mass. Ye et al. [11] conducted two series of physical modeling experiments. Under different grouting process, they conducted physical modeling experiments with or without grouting process and studied the influence of compaction grouting on the performance of compaction-grouted soil nails. A hyperbola-based model was proposed to describe the variation of the pullout force of the model tests with and without grouting.

Combined with a series of research results obtained by domestic and foreign scholars, it has been found that nodular piles have outstanding advantages in bearing capacity. At present, the theoretical research on nodular piles is still immature. Experimental work can simulate the deformation characteristics and bearing characteristics of the nodular piles under specific working conditions, which is an effective method to study and solve this series of problems. However, the model test can only study the variation of some working conditions and parameters, and numerical simulation is often used to study the bearing characteristics of engineering piles under more complex working conditions. By comparing the results of the model test and numerical simulation, the reliable test basis can be provided for the practical engineering design method and design theory of the nodular piles.

In this paper, we analyzed the compressive characteristics of twelve kinds of vortex-compression nodular piles based on the model test [12–14]; ABAQUS finite element numerical simulation software was used to study the compressive characteristics of nodular piles under the influence of multiple parameter changes so as to optimize the parameter design of engineering piles. By modeling the interaction mechanism between fluidized concrete and foundation soil in the expansion process, the deformation equation of foundation soil in the process was established. By further integrating numerical analysis and experimental work, the calculation method of ultimate bearing capacity of vortex-compression nodular pile was derived.

2. Experimental Work

2.1. Material and Pile Model Size. The test piles were 1000 mm long, and their effective length (L_0) was 900 mm with a shaft, diameter (D) of 30 mm. The height and diameter (D_e) of the nodular part are 60 mm and 120 mm, respectively. Based on similarity of the elastic modulus of the materials used under laboratory and real conditions and comprehensively considering the elasticity modulus, stability, and workability of the material, we used the aluminum tube with a wall thickness of 3 mm, and the nodular parts used the nylon resin. Wire of strain gauge was passed through a hole with the diameter of 10 mm in the direction of the nodular part near the pile. Figure 1 presents the detailed configuration of pile.

The detailed size of each pile is shown in Table 1, and N indicates the number of nodular part, H indicates the bottom level of nodular part, and S indicates the spacing between nodular parts.

2.2. Foundation Soil. Sand was used as simulated foundation soil because it is available and easy to prepare. The compactness of sand layer can be controlled, mechanical and geometric properties of which are similar to those foundation soil under actual conditions. After cleaning, the sand was dried and passed through 1 mm and 0.1 mm standard sieves.

Sand was filled into the model box, and the piles were embedded at the same time. Sand loading, measurement, and filling were carried out in layers with soil gauges. Sand was added into the model box, flatten with a flatterer, and then compacted with a self-made compactor to get relative density of 0.67. All layers were filled up with same process.

2.3. Model Box and Loading System. The iron model box is a cylinder, with the wall thickness of 10 mm, inner diameter of 1000 mm, and height of 1200 mm (Figure 2(a)). In order to enhance its stiffness, stiffeners were set in the vertical and horizontal directions of its outer wall. There were four holes in the bottom plate of the model box, and porous stones were set at the bottom of the bottom plate to drain out the supersaturated water from the soil (Figure 2(b)).

Loading frame adopted the portal frame structure (Figure 3(a)). Two columns were connected with the anchor hole by the pedestal rod and the beam to make the reaction frame. Column had box structure with four mounting surfaces, which can be built into various forms according to the test type. The rail was installed on the beam, and the trolley platform also can be installed; the oil cylinder can move along the beam and fixed in any position. In order to control the load and time accurately, this test adopted a double acting cylinder that has the manual adjustment function, which can be connected with the pressure sensor. Its peak load was 100 kN, the working pressure was greater than 25 MPa, the stroke was 150 mm, the manual stroke was 100 mm, and the starting pressure was 0.2 MPa (Figure 3(b)). The manual oil pump had a single output channel, and it can be manually reversed, and its maximum pressure was 63 MPa (Figure 3(c)).

2.4. Data Acquisition. The displacement of pile tip was measured by a numerical control acquisition displacement sensor with an accuracy of 0.01 mm and a range of 100 mm. The dial indicator was set on the load sensor of the pile top and fixed on the specially-made dial indicator frame through the magnetic base.

In order to study the axial force transfer characteristics of pile under compression load, we measured the stress and strain along axis direction of piles under vertical loads, and strain gauges were set in key points (Figure 4) to measure the

(a) (b)

Figure 1: Typical pile structure: (a) P-1 equal-section pile; (b) P-7 nodular pile.

Table 1: The configuration of nodular piles.

Number	L_0 (mm)	D (mm)	D_e (mm)	N	H (mm)	S (mm)
P-1	900	30	—	—	—	—
P-2	900	30	90	—	—	—
P-3	900	30	120	1	−900	—
P-4	900	30	120	1	−810	—
P-5	900	30	120	1	−570	—
P-6	900	30	120	1	−330	—
P-7	900	30	120	2	−330, −630	240
P-8	900	30	120	2	−630, −810	120
P-9	900	30	120	2	−510, −810	240
P-10	900	30	120	2	−390, −810	360
P-11	900	30	120	2	−270, −810	480
P-12	900	30	120	3	−270, −540, −810	210

(a) (b)

Figure 2: (a) The model box. (b) Model box drainage system.

strain of different key points and get the axial force in different depth of the pile, and then we obtained the pile axial force transfer curve [15–17].

2.5. Loading Test Program. In this test, we adopted the Jack loading method [18], according to technical code for testing of building pile foundation; the load was slow and maintained stage by stage. Each stage of load was 1/10–1/15 of the estimated ultimate bearing capacity, and readings were recorded once every 15 minutes within the first hour, every 30 minutes within the second hour, and every 1 hour thereafter. The settlement reaches a stable stage when the settlement at each stage of the load was less than 0.1 mm in the last 30 minutes and next stage of load can be applied. When the ith load was applied, the total settlement $h \geq 40$ mm or the settlement of this load Δh_i was greater than or equal to the 5 times of the last loading stage. Test load can be ended, and the corresponding settlement Δh_{i-1} was taken as the ultimate load of the model pile test. If the total settlement $h < 50$ mm when the ith load is applied, but the settlement still not reach a stable state after 24 h, the loading can also be ended, and the previous load is taken as the ultimate load of this model pile test.

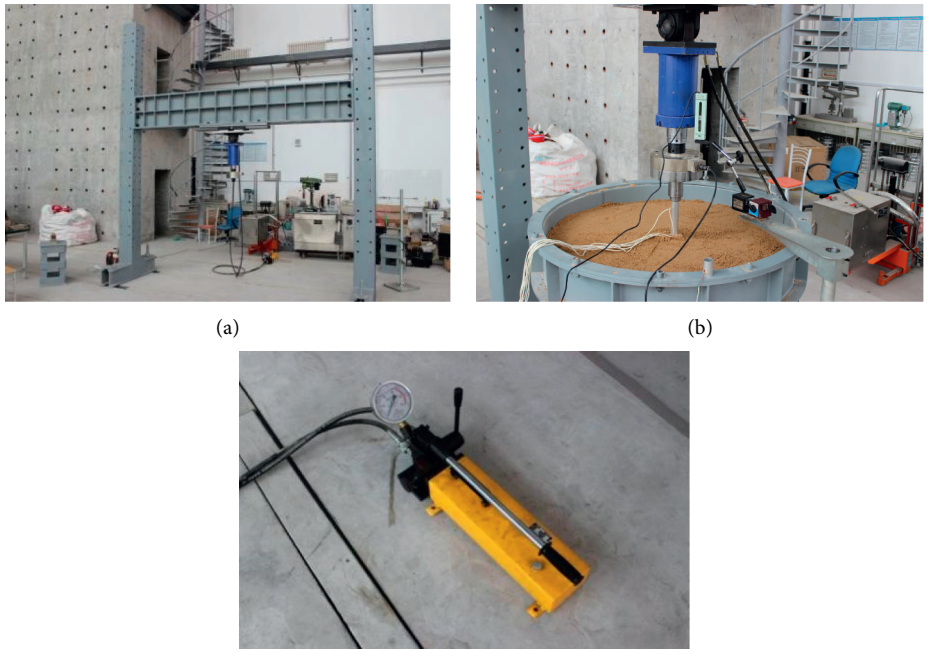

(a) (b)

(c)

Figure 3: Loading device: (a) counter-force rack; (b) double acting cylinder; (c) manipulating fuel pump.

2.6. Results and Discussion

2.6.1. Analysis of Load-Settlement Relationship of Nodular Piles. The load-displacement curves of 12 piles under compressive load are summarized in Figure 5.

P-1 pile is an equal-section pile with the same diameter as that of other nodular piles. The bearing capacity of pile P-2 to P-12 is much larger than that of pile P-1, which indicates that the nodular piles have extraordinary mechanical performance under compressive load compared with equal-section pile.

P-2–P-6 are single piles with one nodular part. P-2 and P-5 have the same nodular part position but different diameter of nodular part. It can be seen that the ultimate bearing capacity of single pile becomes greater with the increase in diameter of nodular part. The position of the nodular part has a great influence on the bearing capacity of single nodular pile. For P-3, P-4, P-5, and P-6, which have different nodular part position, the lower the nodular part is, the higher the ultimate compressive bearing capacity is. Moving the nodular part to the middle part of pile decreases the compressive bearing capacity, and piles with nodular part at the upper part has the minimum compressive bearing capacity. Therefore, it is better to set the nodular part near the bottom of the pile body in the design.

P-7–P-11 are piles with two nodular parts. P-7 and P-9 have the same spacing between nodular parts, but nodular parts are at different positions. Their bearing capacity is not significantly influenced by the position of nodular parts. If one nodular part at the lower part of the pile body is fixed and the position of the upper nodular part is changed, the bearing capacity of pile increases when the upper nodular part is located at higher position. However, the nodular part spacing should not exceed 6 times of the height of nodular part.

P-12 is the pile with three nodular parts, the bearing capacity of which is the largest among the 12 types of pile. The arrangement of its nodular parts is approximately as the composite and superposition of P-6 with single nodular part and P-9 with two nodular parts, and its bearing capacity is also approximately the sum of the bearing capacity of P-6 and P-9. For nodular piles with three nodular parts, if the nodular parts are arranged reasonably, its bearing capacity is approximately the sum of the bearing capacity of one pile with single nodular part and one pile with two nodular parts.

2.6.2. Analysis of Load Transfer Law of Nodular Piles. To accurately measure the data of load transfer and deformation of piles, strain gauges are arranged at the nodular part and key parts of the pile. The axial force transfer curves of twelve kinds of piles under the compressive load are summarized in Figure 6.

The axial force of P-1 is constant under the action of ultimate load. This may be due to use of sand as soil material and aluminum tube as pile body material, which decrease the friction coefficient and thus the load is almost entirely borne by the pile end.

Under the action of ultimate load, the axial force of the upper part of P-3 at the nodular part changed very slightly, indicating that the load is mainly borne by the nodular part at the pile end, and its compressive bearing capacity is relatively large.

The axial force of the rest piles increases at the position of the nodular part. The axial force at position below the nodular part is significantly reduced, indicating that the nodular parts play a great role in bearing the compressive load.

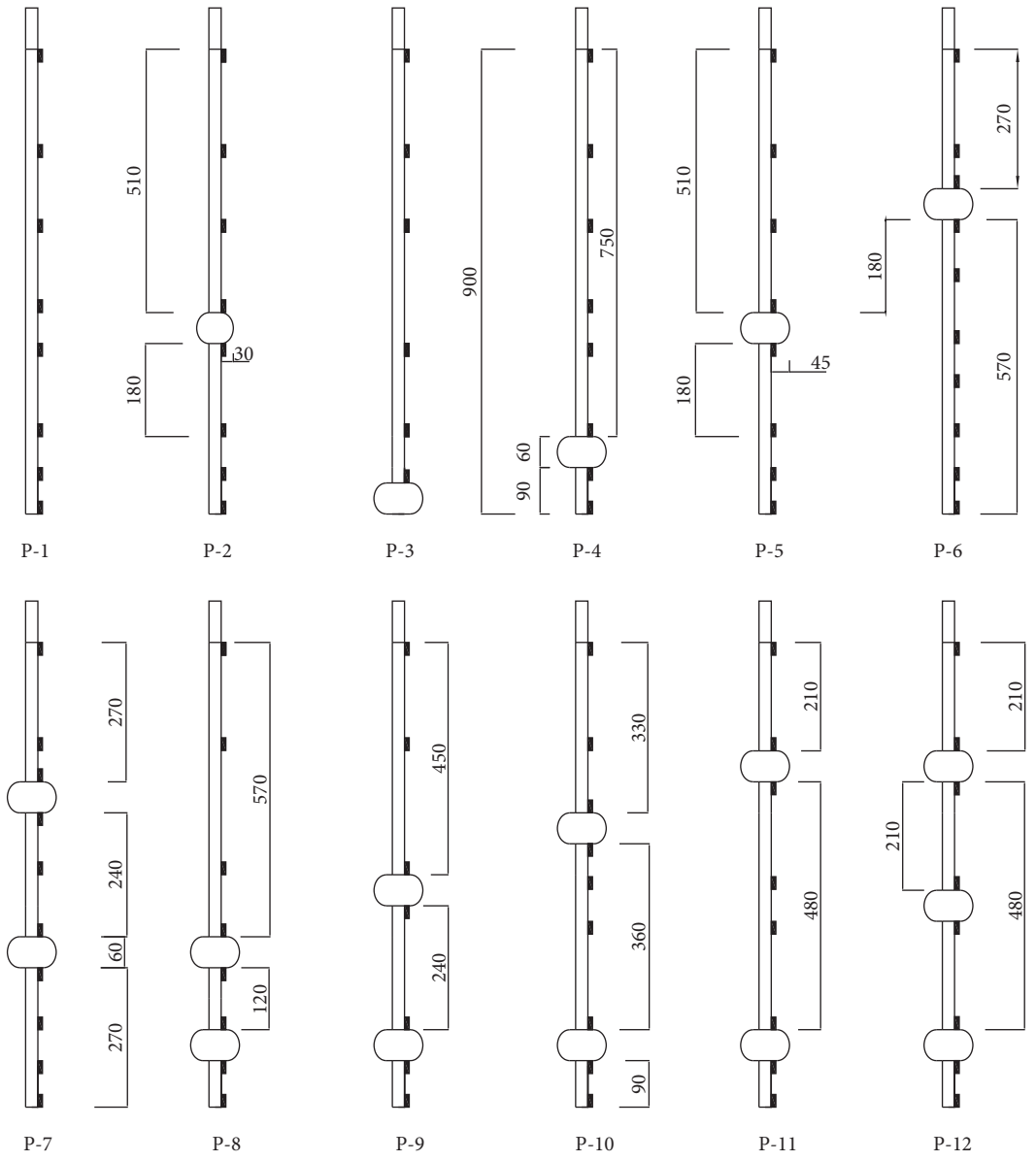

Figure 4: Strain gauge paste location map.

Under the ultimate load, the load transfer of equal-section pile is basically linear. For monopile with one nodular part, with the higher position of nodular part, the decrease in the axial force at the nodular part becomes slighter. For monopile with two nodular parts, when the nodular part spacing is small, the decrease in axial force at its lower nodular part is similar to that of pile with one nodular part. However, the decrease in axial force at its upper nodular part decreases with the increasing of nodular part spacing. For monopile with three nodular parts, the decrease in axial force at each nodular part becomes slighter from top to bottom.

3. Numerical Modeling

3.1. Unit Selection

3.1.1. Constitutive Model of Pile Material. Since the elastic modulus of aluminum is close to that of concrete and the material uniformity is relatively good, the aluminum tube was adopted as the material for making the model pile, whose strength and stiffness are much stronger than those of surrounding soil. The stiffness of the nodular part is much stronger than that of the soil around the pile. For the convenience of calculation, the material property of the nodular part was regarded as the same as aluminum. Under vertical load, the failure of pile foundation is usually controlled by settlement and shear slip of soil around pile, and the failure of the pile body rarely occurs. Therefore, the linear elastic model was adopted for the pile body [19], and the constitutive relation of its tensor form can be expressed as follows [20]:

$$\sigma_{ij} = \left[\frac{2G\mu}{1-2\mu}\delta_{ij}\delta_{kl} + G\left(\delta_{ik}\delta_{jl} + \delta_{il}\delta_{jk}\right)\right]\varepsilon_{kl} = D_{ijkl}\varepsilon_{kl}, \quad (1)$$

where D_{ijkl} is the component of the elastic tensor, which can be expressed as follows:

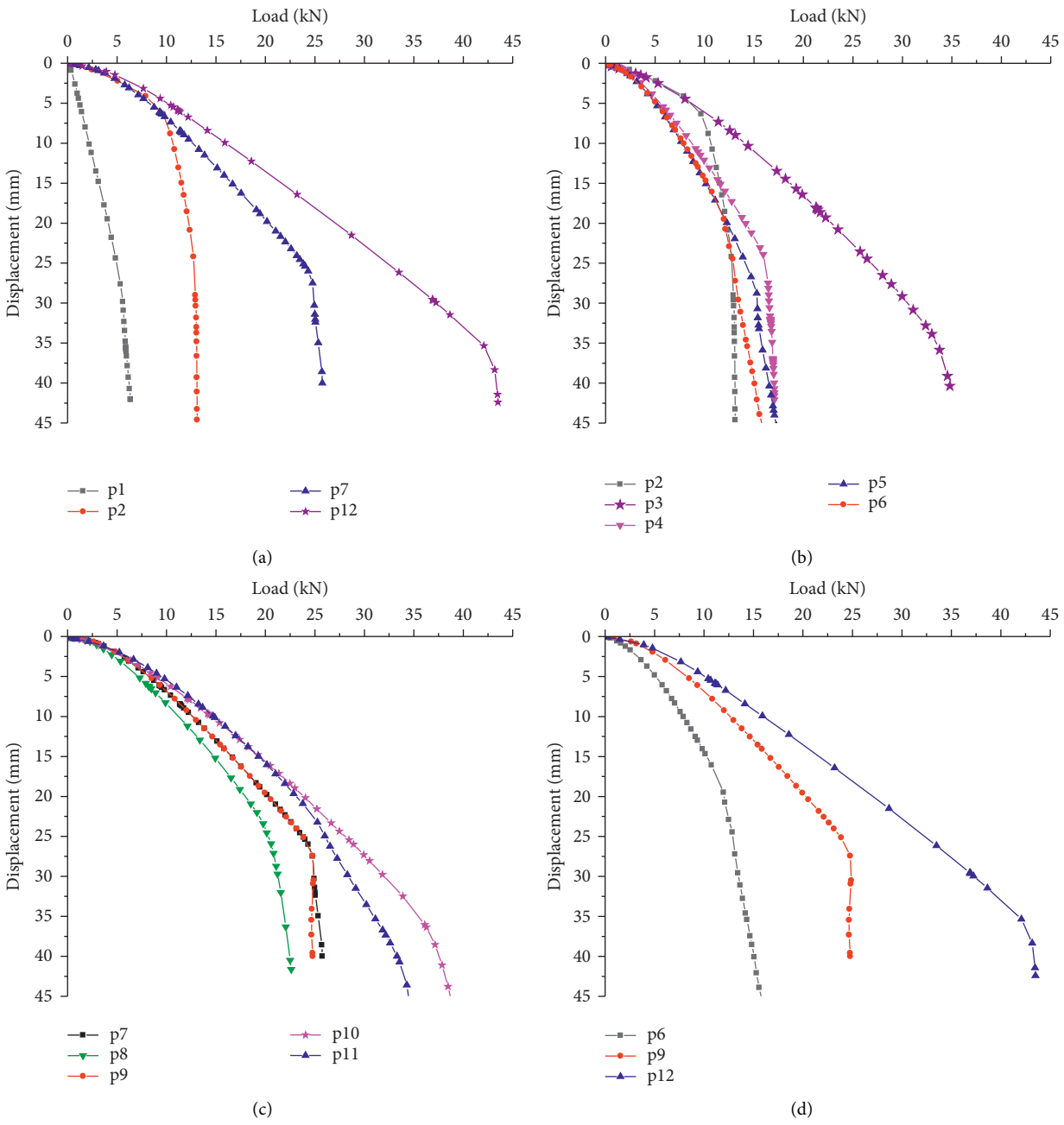

Figure 5: Load-displacement curves of 12 kinds of pile under compressive load: (a) equal-section pile and nodular piles; (b) piles with one nodular part; (c) piles with two nodular parts; (d) piles with different nodular parts.

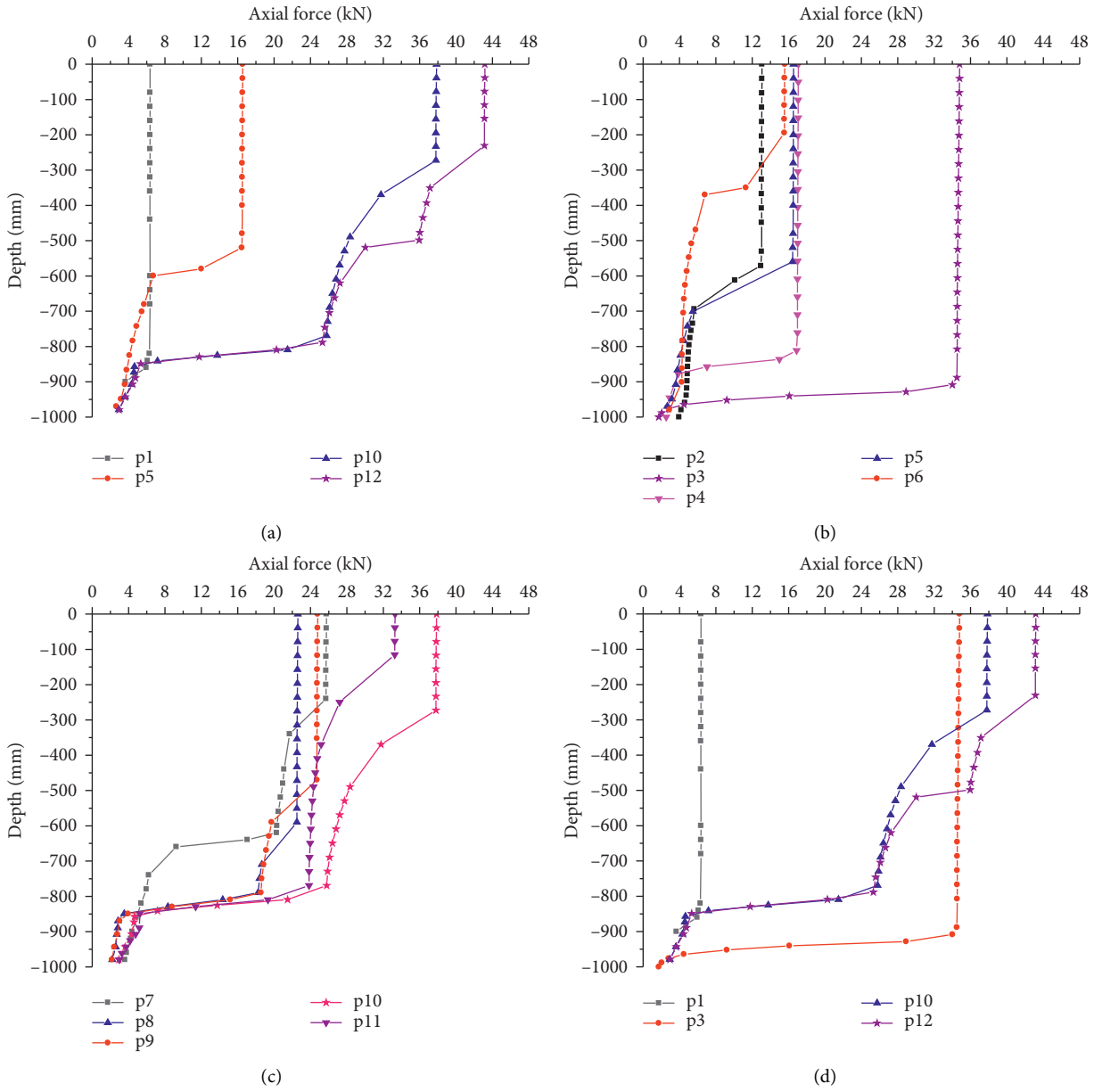

FIGURE 6: Axial force transfer curve of 12 kinds of pile under the action of ultimate compressive load: (a) equal-section pile and nodular piles; (b) piles with one nodular part; (c) piles with two nodular parts; (d) piles with different nodular parts.

$$[D] = \frac{E}{(1+\mu)(1-2\mu)} \begin{bmatrix} 1-\mu & \mu & \mu & 0 & 0 & 0 \\ & 1-\mu & \mu & 0 & 0 & 0 \\ & & 1-\mu & 0 & 0 & 0 \\ & & & \frac{1}{2}-\mu & 0 & 0 \\ & \text{sym} & & & \frac{1}{2}-\mu & 0 \\ & & & & & \frac{1}{2}-\mu \end{bmatrix}, \tag{2}$$

where E is the elastic modulus of the material, μ is the Poisson's ratio, and $G = E/2(1+\mu)$.

3.1.2. Constitutive Model of Soil Material. The σ-ε relationship of the soil around the pile shows significant nonlinear and plastic characteristics under load. For isotropic hardening materials, assuming that the loading function is known as Φ, the plastic scalar factor $d\lambda$, the plastic potential function Q, and the hardening modulus are expressed as follows [21]:

$$\phi\left(\sigma_{ij}, H\right) = 0, \tag{3}$$

$$Q = Q\left(\sigma_{ij}, H\right) = 0, \tag{4}$$

$$d\lambda = \frac{1}{A}\frac{\partial \phi}{\partial \sigma_{ij}} d\sigma_{ij}, \tag{5}$$

$$A = -\frac{\partial \phi}{\partial H\alpha}\frac{\partial H\alpha}{\partial \varepsilon_{ij}^{p}}\frac{\partial Q}{\partial \sigma_{ij}}. \tag{6}$$

According to the elastic-plastic principle, the elastic strain part and the plastic strain part constitute the total strain variables of soil mass, and their incremental expression is as follows:

$$d\varepsilon_{ij} = d\varepsilon_{ij}^{e} + d\varepsilon_{ij}^{p}, \tag{7}$$

where $d\varepsilon_{ij}^{e}$ is the elastic strain, $d\varepsilon_{ij}^{e} = [C_{ijkl}^{e}]d\sigma_{kl}$, $d\varepsilon_{ij}^{p}$ is the plastic strain, and $d\varepsilon_{ij}^{p} = \lambda(\partial Q/\partial \sigma_{ij})$. Substitute $d\varepsilon_{ij}^{e}$ and get $d\varepsilon_{ij}^{p}$ in the following formula:

$$d\sigma_{ij} = D_{ijkl}^{e}\left[d\varepsilon_{kl} - d\lambda\frac{\partial Q}{\partial \sigma_{ij}}\right]. \tag{8}$$

When the material is isotropic, equation (9) holds. Substituting equations (8) and (9) into equation (6), equation (10) can be obtained:

$$d\phi = \frac{\partial \phi}{\partial \sigma_{kl}} d\sigma_{kl} + \frac{\partial \phi}{\partial H}\frac{\partial H}{\partial \varepsilon_{kl}^{p}} d\varepsilon_{kl}^{p}, \tag{9}$$

$$\frac{\partial \phi}{\partial \sigma_{ij}} D_{ijkl}^{e} - \frac{\partial \phi}{\partial \sigma_{mn}} D_{mnpq}^{e} d\lambda \frac{\partial Q}{\partial \sigma_{pq}} - A d\lambda = 0. \tag{10}$$

By substituting (9) into (5), the general expression of isotropic hardening $d\lambda$ is obtained:

$$d\lambda = \frac{\left(\partial \phi/\partial \sigma_{ij}\right) D_{ijkl}^{e} d\varepsilon_{kl}}{A + \left(\partial \phi/\partial \sigma_{mn}\right) D_{mnpq}^{e}\left(\partial Q/\partial \sigma_{pq}\right)}. \tag{11}$$

By substituting equation (11) into equation (5), the general expression of elastic-plastic of isotropic materials can be obtained:

$$d\sigma_{ij} = \left[D_{ijkl}^{e} - \frac{\left(\partial \phi/\partial \sigma_{ab}\right) D_{ijab}^{e} D_{cdkl}^{e}\left(\partial \phi/\partial \sigma_{cd}\right)}{A + \left(\partial \phi/\partial \sigma_{mn}\right) D_{mnpq}^{e}\left(\partial Q/\partial \sigma_{pq}\right)}\right] d\varepsilon_{kl}. \tag{12}$$

The More–Coulomb model is generally used to describe soil yield; the More–Coulomb yield surface is a pyramid in the principal stress space and an equilateral hexagon on the π plane but not equiangular. The More–Coulomb yield condition can be expressed as follows:

$$\begin{aligned} &\frac{1}{3} I_1 \sin\varphi + \sqrt{J_2}\sin\left(\theta + \frac{\pi}{3}\right) + \frac{\sqrt{3J_2}}{3}\cos\left(\theta + \frac{\pi}{3}\right) \\ &\quad \sin\varphi - C\cos\varphi = 0, \end{aligned} \tag{13}$$

where θ can be expressed by $\cos 3\theta = \sqrt{2}J_3/\tau_8^3$, I_1 is the first invariant of the stress tensor, J_2 is the second invariant of stress deviator, J_3 is the third invariant of stress deviator, and τ_8 is the shear stress of the octahedron. The ultimate shear strength of soil on any force surface can be expressed by Coulomb's law:

$$\tau_n = C + \sigma_n tg\varphi, \tag{14}$$

where φ is the angle of internal friction, C is the cohesion and its value is the intercept of the failure line on the vertical axis, and τ_n is the normal stress (on the stress surface).

According to Figure 7, it can be seen that

$$\begin{aligned} \tau_n &= R\cos\varphi, \\ \sigma_n &= \frac{1}{2}\left(\sigma_x + \sigma_y\right) - R\sin\varphi, \\ R &= C\cos\quad \varphi + \frac{1}{2}\left(\sigma_x + \sigma_y\right)\sin\varphi, \end{aligned} \tag{15}$$

where R is the radius of the Mohr stress circle and $R = [(1/2)(\sigma_x + \sigma_y)^2 + \tau_{xy}^2]^{1/2}$.

3.1.3. Pile-Soil Contact Model. In order to simulate the interaction between nodular piles and soil around the pile, contact elements should be set on the contact surface between pile and soil. The contact relationship between pile and soil is complex and nonlinear. Normally, when two contact surfaces contact each other and slide or move relative to each other, there will be normal contact stress and shear stress between the two contact surfaces. For tangential effect, a commonly used friction model in ABAQUS is Coulomb friction [22, 23]. The calculation formula of Coulomb friction is as follows:

$$\tau = \mu p, \tag{16}$$

where τ is the critical tangential stress, μ is the coefficient of friction, and p is the normal contact compressive stress.

Before the tangential force reaches the critical shear stress, there will be no relative slip between the friction surfaces or between pile and soil, which is called sticking state. After the tangential force reaches the critical stress, relative slip will occur on the contact surface between pile and soil, which is called slipping state. If the two states of sticking and slipping are discontinuous, the penalty function formula in ABAQUS can be used to realize the transition between the two states. The penalty function formula allows

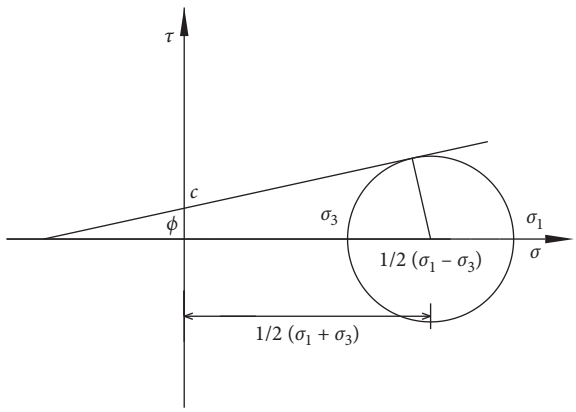

Figure 7: More–Coulomb failure criterion.

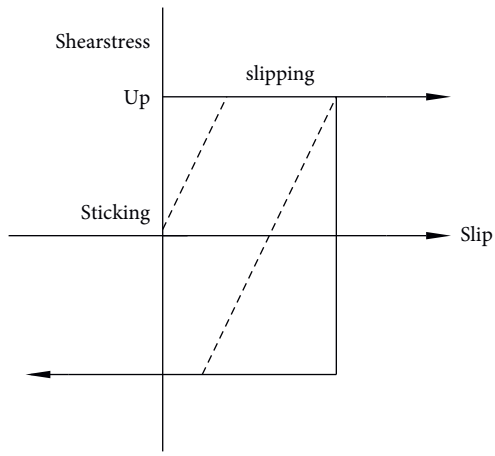

Figure 8: Concept description of elastic slip.

elastic slip, the concept of which is described in Figure 8. When the friction force between two contact surfaces is less than τ_{max}, the two contact surfaces are sticking; if there is relative friction between two contact surfaces, the calculation program will automatically define the reasonable penalty stiffness. During the numerical simulation, the program will automatically use the attenuation index method to simulate the transition between sticking and sliding state [24, 25].

3.2. Model Dimensions and Parameters. The main purpose of numerical simulation is to study the influence of geometric parameters of vortex-compression nodular pile on its compressive characteristics and soil around the pile. By changing the geometric parameters such as the size, the number, the bottom elevation, and the distance between nodular parts, the influence on the bearing capacity of vortex-compression nodular piles and the soil around the pile was studied. Twelve kinds of model sizes (P-1–P-12) were adopted, which are the same as those in the model test.

The physical and mechanical parameters of the model pile and soil around the pile were determined by laboratory tests, and the specific data are shown in Table 2.

3.3. Boundary Conditions and Grid Division. By taking a two-dimensional axisymmetric model, freedom in the Y direction was constrained at the bottom of the soil, freedom in the X direction was constrained on both sides of the soil, and freedom in the horizontal direction of the pile body was constrained. The axisymmetric 4-node element was used for the pile body and soil around the pile. The strain gradient of stress of the soil in and surrounding nodular parts was relatively large, so the grid should be partly densified. Pile P-1, P-5, P-7, and P-12 were typical grid division of nodular piles with different numbers and diameters of nodular part, and the scheme is shown in Figure 9 [26–28].

3.4. Results and Discussion

3.4.1. Analysis of Failure Morphology of Foundation Soil of Compressed Nodular Piles. The plastic strain and displacement of 12 kinds of pile under 50%, 75%, and 100% ultimate load were extracted, and the plastic strain and displacement contour were summarized [29], where the displacement contour of P-10 pile under compressive loading can be seen in Figure 10 and plastic strain contour of P-10 pile under compressive loading can be seen in Figure 11. By comparing with the simulation results of typical piles with different numbers of nodular part, the preliminary conclusions were as follows.

During the loading process of non-nodular piles, no significant deformation and displacement occurred on pile side foundation, and the soil on pile end was significantly compressed. The ultimate failure pattern was local shear failure.

The displacement and plastic strain of the pile with single nodular part changed greatly, which showed the characteristics of two fulcrum end bearing friction pile. With the increase in axial compression load, the soil under the nodular part was gradually compressed, and most of the load was borne by the nodular part instead of the pile end. The retaining force at the pile end lagged behind that at the nodular part, and local shear failure occurred successively in the soil under the nodular part and the soil at the pile end. The soil above the nodular part detached from the nodular part, and the detachment is about 3/4–1 times the height of the nodular part under ultimate load.

For the piles with small distance between two nodular parts, the stress was mainly concentrated at the bottom of the lower nodular part under ultimate load, and soil compression and local shear failure occurred at the bottom and pile ends of the lower nodular part. There was no detachment of pile and soil in the upper soil of the lower nodular part, the upper and lower nodular parts, and the soil in between constituted a new nodular part. Piles with two nodular parts and a wide distance between nodular parts showed the characteristics of three fulcrum end bearing friction pile under the ultimate load, and soil compression and local shear failure occurred at the bottom and pile ends of the two nodular parts. The plastic failure zone of foundation soil at pile end was obviously smaller than that at the nodular parts, and the plastic failure zone of the upper nodular part is obviously smaller than that of the lower part. Detachment of pile and soil occurred in the upper soil at the upper and lower nodular

Table 2: Physical and mechanical parameters of model piles and soil around pile.

Model material	Constitutive model	Density (g/cm^3)	Shear modulus (MPa)	Poisson's ratio (MPa)	Cohesion (kPa)	Internal friction angle (°)
Model pile	Elastic model	2.7	4.0×104	0.25	—	—
Soil around pile	Moore Coulomb	1.8	20	0.33	4	30

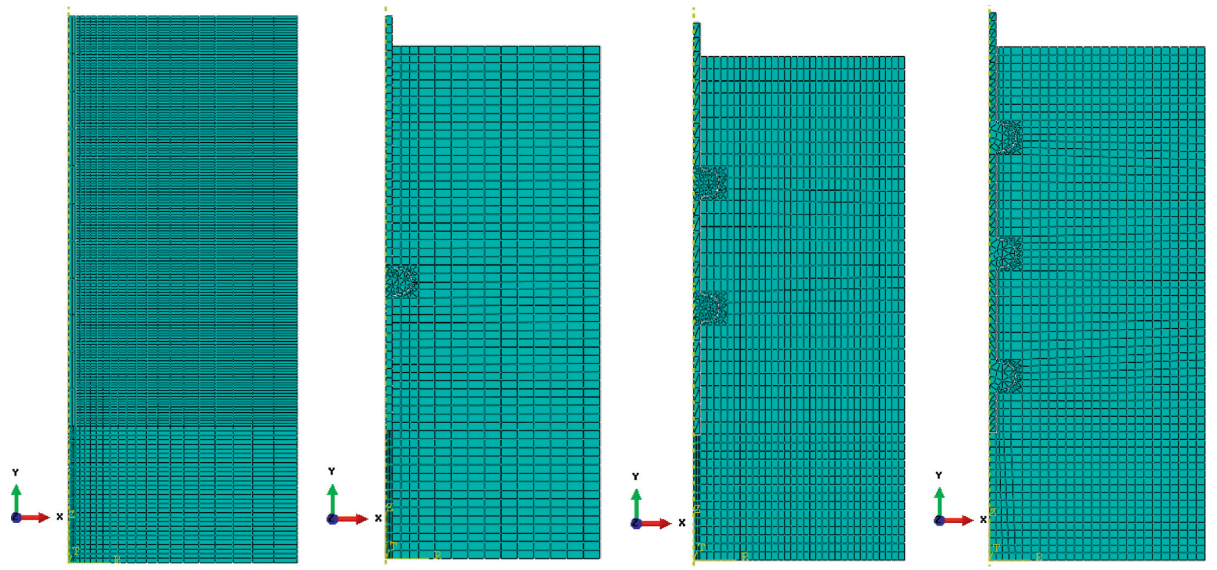

Figure 9: FEM models of expanding pile with different expanding sections and diameter: (a) P-1 pile; (b) P-5 pile; (c) P-7 pile; (d) P-12 pile.

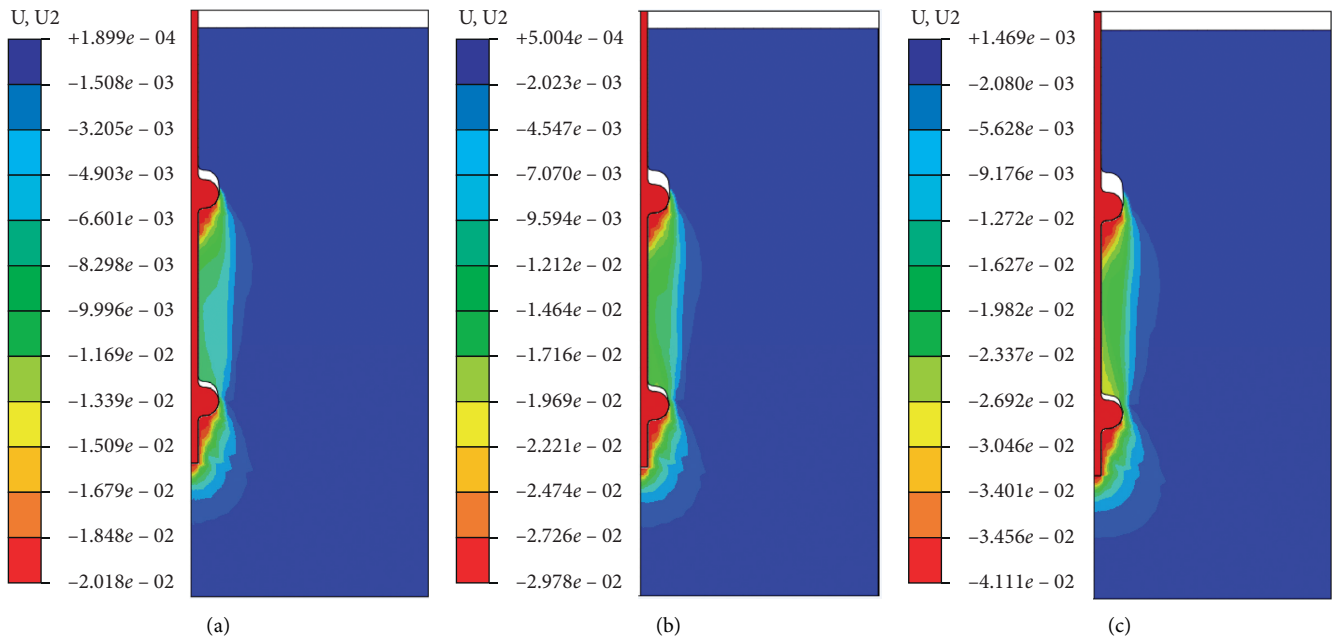

Figure 10: Displacement contour of P-10 pile under compressive loading: (a) 50% ultimate load; (b) 75% ultimate load; (c) 100% ultimate load.

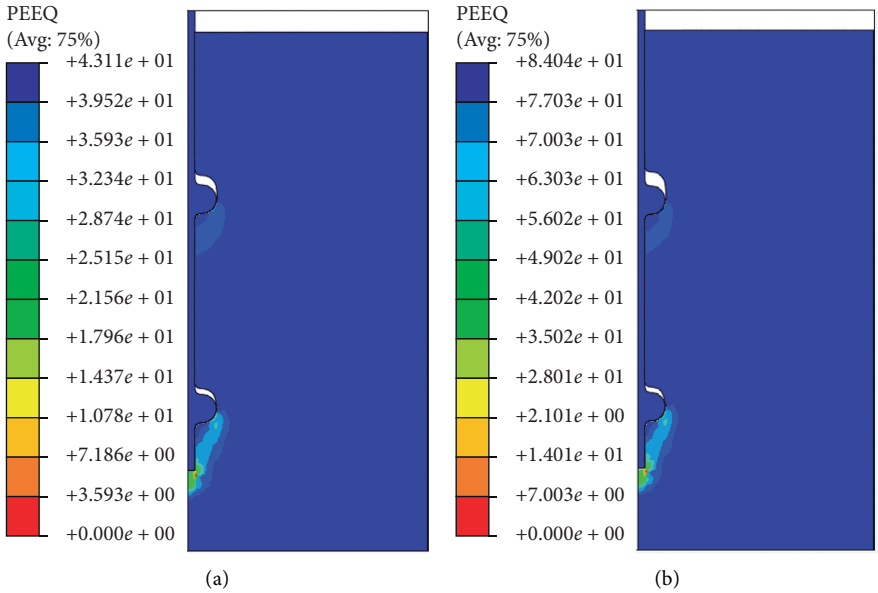

Figure 11: Plastic strain contour of P-10 pile under compressive loading: (a) 50% ultimate load; (b) 75% ultimate load; (c) 100% ultimate load.

parts, and the distance was about 3/4 the height of the nodular part, while the detachment distance at the lower nodular part was slightly less than that at the upper part. When the distance between nodular parts was greater than or equal to 3 times the diameter of the nodular part or 6 times the height of the nodular part, the two nodular parts can work independently. When the distance between nodular parts was less than 3 times the diameter of the nodular part or 6 times the height of the nodular part, the two nodular parts and the soil in between constituted a new nodular part.

Piles with multi nodular parts showed characteristics of four fulcrum bearing friction pile. Under the ultimate load, soil compression and local shear failure occurred at the lower part and pile end of the bottom nodular part. With the increase in axial compression load, plastic failure zones were constituted, respectively, under the three nodular parts, and the range of plastic failure zone increased gradually from top to bottom, with the bearing ratio of the pile end decreasing obviously. There was no detachment of pile and soil in the upper soil of the lower and middle nodular parts; the soil between the upper and lower nodular parts and the three nodular parts constituted a new nodular part.

3.4.2. Analysis of Load-Settlement Relationship of Nodular Piles. Key load points were selected to conduct pile top displacement, and the numerical simulation results of load-displacement of nodular pile tip were summarized in Figure 12. By comparing the load-displacement curves of 12 kinds of pile in Figure 12, the following conclusions could be drawn:

The ultimate bearing capacity of nodular pile was much larger than that of equal-section pile, and the nodular pile has a significant mechanical advantage when bearing compressive load compared with pile with straight shaft. For piles with single nodular part, the position of the nodular part had a great influence on the bearing capacity of single nodular pile, and it is better to set the nodular part near the bottom of the pile body in the design. When the nodular part is in the same position, the ultimate bearing capacity of single pile was large when the diameter of its nodular parts was long. For piles with double nodular part, the position of the nodular part has little influence on the bearing capacity of single pile when the distance between their nodular parts was the same. For piles with three nodular parts, if the distance between nodular parts was arranged reasonably, its bearing capacity was approximately the sum of the bearing capacity of one pile with single nodular part and two piles with two nodular parts. The numerical simulation results are in agreement with the experimental results, which further confirms the experimental conclusion.

3.4.3. Analysis of Load Transfer Law of Nodular Piles. The axial force of the pile body under the ultimate load was selected, and in order to accurately describe the load transfer law of each type of pile, many reference points were selected on each type of pile. The axial force transfer curves of 12 types of pile under compression load were summarized in Figure 13. According to Figure 13, the variation rule of pile axial force under the ultimate load was summarized.

Under the ultimate load, the load transfer of equal-section pile (P-1) was basically linear. For pile with one nodular part (P-2, P-3, P-4, P-5, and P-6), with the enhancement of nodular part position, the decreasing range of the axial force at the nodular part decreased gradually. For pile with two nodular parts, when the spacing between nodular parts was small, the decreasing range of axial force at its lower nodular part was similar to that of single pile with one nodular part, while the decreasing range of axial force at

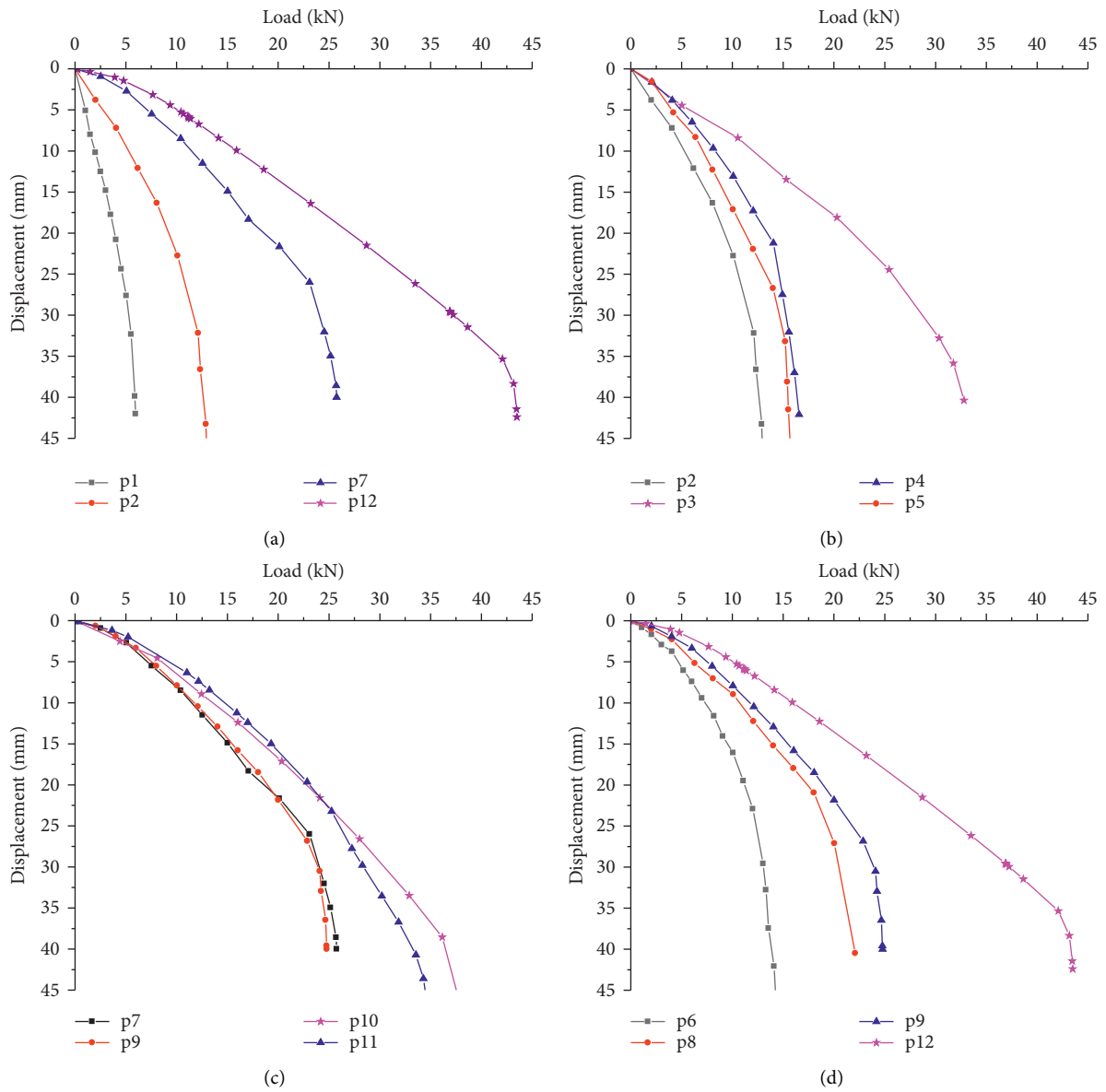

Figure 12: Load-displacement curve of 12 kinds of pile under compressive load: (a) equal-section pile and nodular piles; (b) piles with one nodular part; (c) piles with two nodular parts; (d) piles with different nodular parts.

its upper nodular part decreased with the increasing of the distance. For pile with three nodular parts, the decrease range of axial force of the upper and lower nodular part decreased gradually from top to bottom. The numerical simulation results are in agreement with the experimental results, which further confirms the experimental conclusion.

4. Calculation Method of Ultimate Bearing Capacity

Under compression load, due to the structure of local nodular parts of vortex-compression nodular piles, the soil around the pile presented a series of complex deformation, such as compression, sliding, and pile-soil detachment. The failure mode was quite different from that of compression or shear failure of the traditional pile foundation. Due to the special action mode of the local nodular parts of nodular piles and soil around the pile, pile lateral friction is an important variable affecting its ultimate bearing capacity. Pile lateral friction calculation is relatively complex, which needs to be estimated in combination with quantitative data such as pile bearing deformation and load transfer and modified according to engineering data.

The calculation method adopts the simplified model of effective pile length to estimate the contribution of the pile body and each part of the nodular part to the ultimate load [30]. According to the results of theoretical analysis and numerical simulation, the ultimate bearing capacity of single nodular pile made of reinforced concrete was calculated by taking the change of the number of and the distance between nodular parts into consideration.

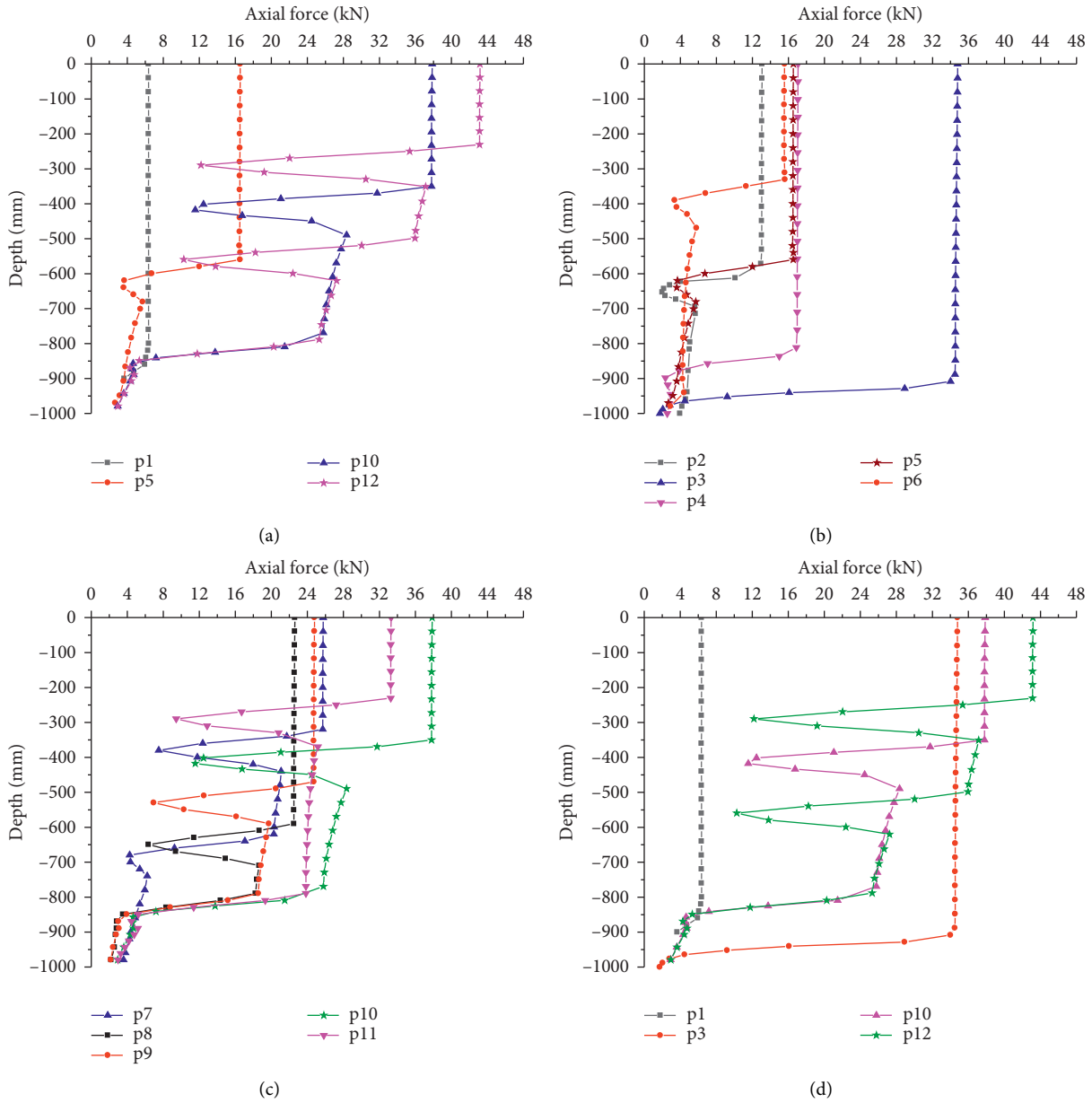

FIGURE 13: Axial force transfer curve of 12 kinds of pile under the action of ultimate compressive load: (a) equal-section pile and nodular piles; (b) piles with one nodular part; (c) piles with two nodular parts; (d) piles with different nodular parts.

The calculation method of pile end bearing capacity of nodular piles is the same as that of traditional straight pile, namely, $F_t = f_t(\pi d^2/4)$, and f_t is the friction coefficient of pile tip.

4.1. Calculation of the Bearing Capacity of Piles with Single Nodular Part

4.1.1. Calculation of the Bearing Capacity of the Curve Section of Nodular Parts. According to the slip line theory, the failure of soil in the circular arc line area below the nodular part belongs to slippage failure, and the slip deformation field in the Prandtl zone was established [31, 32], as shown in Figure 14:

The range of the strain field in the Prandtl zone is bounded by the logarithmic helix that follows $r = R_0 e^{\theta \tan \varnothing}$ and two radial rays $\theta = 0$ and $\theta = \Theta$, and the internal work D_1 is expressed as follows:

$$D_1 = \frac{1}{2} bc \cot \phi R_0 u_0 \tan \phi \left(e^{2\theta \tan \phi} - 1\right), \quad (\theta = \Theta). \tag{17}$$

If the soil outside the strain field of Prandtl zone is assumed to be static, then the boundary line is a discontinuous line, the angle formed between the discontinuity line and the displacement vector is $\varnothing$, and the internal work D_2 of the discontinuity line is expressed as follows:

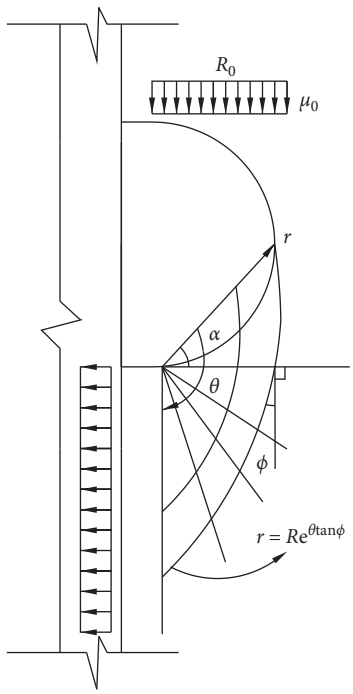

Figure 14: Slip displacement in the Prandtl region around the extended lower soil mass.

$$D_2 = bc\cot\varnothing\int u\mathrm{d}s = bc \cdot \cot\varnothing\int_0^{\theta} u_0 e^{\theta\tan\varnothing}\frac{r\mathrm{d}\theta}{\cos\varnothing}. \tag{18}$$

Because $r = R_0 e^{\theta\tan\varnothing}$ and $D_1 = D_2$, the total internal work is expressed as follows:

$$D = D_1 + D_2 = bc\cot\varnothing R_0 u_0\left(e^{2\theta\tan\varnothing} - 1\right), \quad (\theta = \Theta). \tag{19}$$

In Figure 14, in the strain field of the soil in the lower failure area of the nodular part, $\Theta = 90^\circ + \alpha$. According to the principle of virtual work, external work D_e equals to internal work D_i, and thus the following formula holds

$$F_n = c\cot\varnothing R_o\left(e^{\theta\tan\varnothing} - 1\right), \tag{20}$$

where F_n is the ultimate bearing capacity of soil per unit width of the lower curve section of the nodular part, D is the diameter of the nodular part, d_2 is the diameter of the straight segment of the nodular part, c is the cohesion coefficient of soil around the pile, $\varnothing$ is the internal friction angle of soil around the pile, and F_{cn} is the ultimate bearing capacity of curve section of the nodular part.

$$F_{\mathrm{cn}} = 2F_n\pi\left(\frac{D + d_2}{2}\right) = \pi(D + d_2)c \cdot \cot\varnothing R_0\left(e^{2\theta\tan\varnothing} - 1\right). \tag{21}$$

Under the vertical load, the soil in the lower curve section of the nodular part is not only shear failure but slippage failure based on shear failure. According to the slip line theory, the bearing capacity of the curve section of the nodular part is not only determined by the diameter of the nodular part but also determined by the diameter of the straight section of the nodular part, the cohesion coefficient c of the soil around the pile, and the internal friction angle of the soil around the pile. Compared with the traditional formula, equation (21) can objectively reflect the stress state of the curve section of the nodular part.

4.1.2. Calculation of Side Friction Force of Nodular Piles. As shown in Figure 15, due to the existence of horizontal tensile stress in the L_a area in the upper part of the nodular part, the soil around the pile was detached from the pile body. In case of sliding failure, the soil in L_b range around the pile in the lower part of the nodular part would show compression and deformation, and the horizontal compressive stress would increase accordingly. The expansion coefficient of side friction force is set as γ [33], so the calculation expression of side friction force is expressed.

$$F_{\mathrm{sf}} = f_s\pi dL_0 = f_s\pi d(L - H - L_a + \gamma L_b), \tag{22}$$

$$L_o = L - H - L_a + \gamma L_b, \tag{23}$$

where F_{sf} is the side friction force of nodular piles, f_s is the friction coefficient of pile side, L_0 is the actual effective pile length calculated by side friction force, H is the height of the nodular part, L_a is the area where the horizontal tensile stress exists in the upper part of the nodular part, L_b is the area where the horizontal compressive stress increases in the lower part of the nodular part, and γ is the expansion coefficient and usually taken as 1.1-1.2.

Compared with the traditional empirical formula, formula (22) uses the effective length conversion model to calculate the pile side friction resistance, and the calculated length of the pile side friction resistance is not the total pile length minus the height of nodular part. There was no side friction force in the local area on the pile side in the upper part of the nodular part, while the friction resistance in the local area on the pile side in the lower part of the nodular part increased.

4.1.3. Calculation of Ultimate Bearing Capacity of the Pile with Single Nodular Part. Combined with the above analysis, the contribution of the nodular part and the pile side friction force to the bearing capacity of the whole single pile was quantitatively corrected. The effective length L_0 was used to calculate the pile side friction force, and the slip line theory was used to calculate the bearing capacity of the curve section of the nodular part. Thus, the ultimate bearing capacity of the pile with single nodular part was calculated as follows:

$$F_u = F_t + F_{\mathrm{cn}} + F_{\mathrm{sn}} + F_{\mathrm{sf}}, F_u < F_p^c, \tag{24}$$

where the bearing capacity of the straight section of the nodular part is $F_{\mathrm{sn}} = f_t(\pi(d_2^2 - d_1^2)/4)$, $F_p^c = F_c^c + F_r^c$, F_p^c is the bearing capacity of the pile body, F_c^c is the bearing

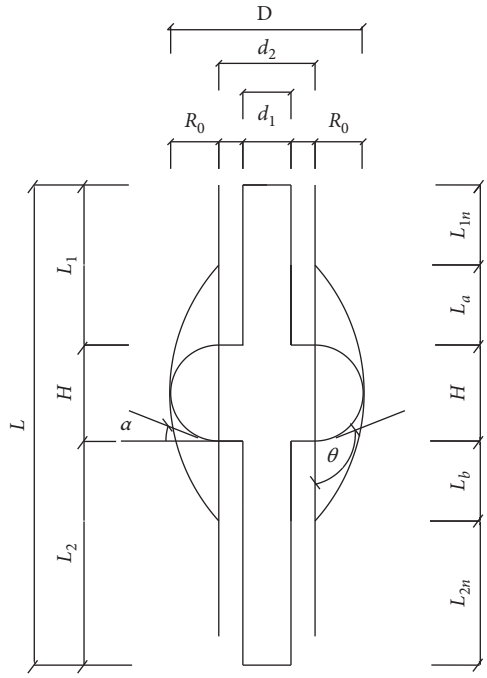

Figure 15: Single expansion section of compressive pile.

capacity of concrete, and F_r^c is the bearing capacity of reinforced.

4.2. Calculation of Bearing Capacity of the Pile with Two Nodular Parts. When $S \geq 3D$, that is, when the distance between the nodular parts is large, it will show the failure pattern in Figure 16. When $S < 3D$, that is, when the distance between the nodular parts is small, the failure pattern in Figure 17 will appear.

4.2.1. When $S \geq 3D$, Calculation of Bearing Capacity of Compressive Pile with Two Nodular Parts. When $S \geq 3D$, the influence between the upper and lower nodular parts is negligible, and the failure pattern of soil around the upper and lower nodular parts is similar to that of piles with single nodular part. Therefore, the bearing capacity calculation method of the nodular parts of the pile with two nodular parts can be regarded as the sum of the bearing capacity of two nodular parts.

$$F_u = F_t + 2F_{\text{cn}} + 2F_{\text{sn}} + F_{\text{sf}}, F_u < F_p^c, \tag{25}$$

where $F_{sf} = f_s \pi d_1 L_0 = f_s \pi d_1 \ (L - H_1 - H_2 - L_{a1} - L_{a2} + \gamma_1 L_{b1} + \gamma_2 L_{b2})$; the calculation formula of $F_{\text{cn}}, F_{\text{sn}}$, and F_p^c is the same as that of the pile with single nodular part.

4.2.2. When $S < 3D$, Calculation of Bearing Capacity of Compressive Pile with Two Nodular Parts.

$$F_u = F_t + F_{\text{lcn}} + F_{\text{lsn}} + F_{\text{sf}} + F_{\text{ln}}, F_u < F_p^c, \tag{26}$$

where F_{ln} is the pile lateral friction resistance of nodular part, F_{lcn} is the ultimate bearing capacity of curve section of the lower nodular part, F_{lsn} is the bearing capacity of the straight section of the lower nodular part, $F_{\text{sf}} = f_s \pi d_1 L_0 = f_s \pi d_1 \ (L_1 + L_2 - L_{a1} + \gamma_2 L_{b2})$, and $F_{\text{ln}} = f_{\text{lf}} \pi \ DL_0 = f_{\text{lf}} \pi D \ (S_n + ((H_1 + H_2)/2))$, and the calculation formula of

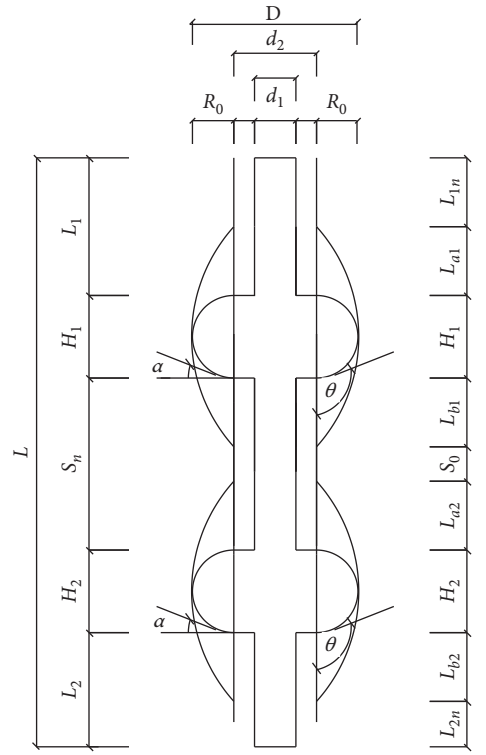

Figure 16: $S \geq 3D$, pile with two nodular parts.

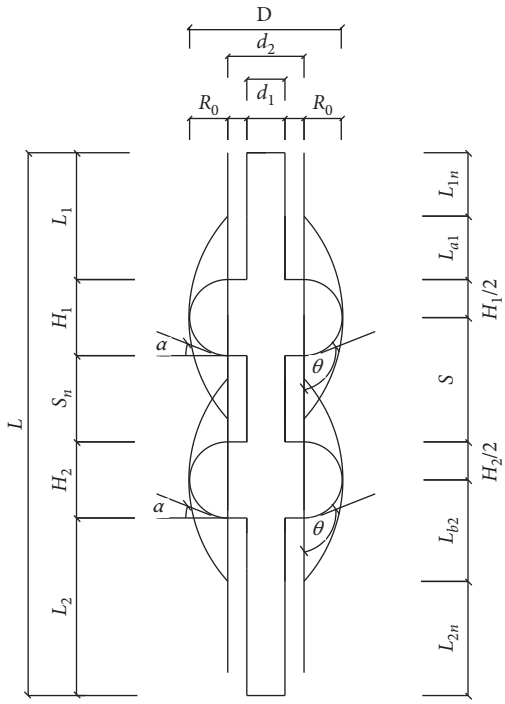

Figure 17: $S < 3D$, pile with two nodular parts.

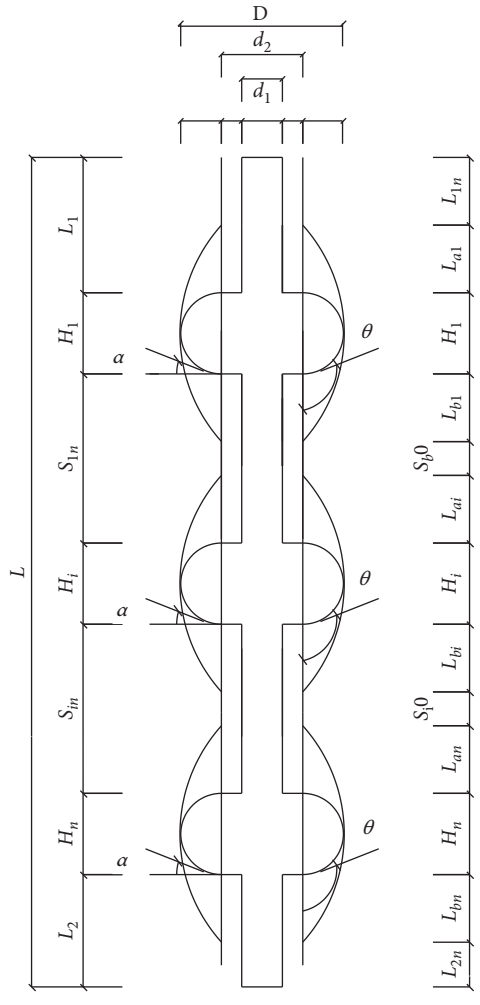

Figure 18: $S_i \geq 3D$, pile with multiple nodular parts.

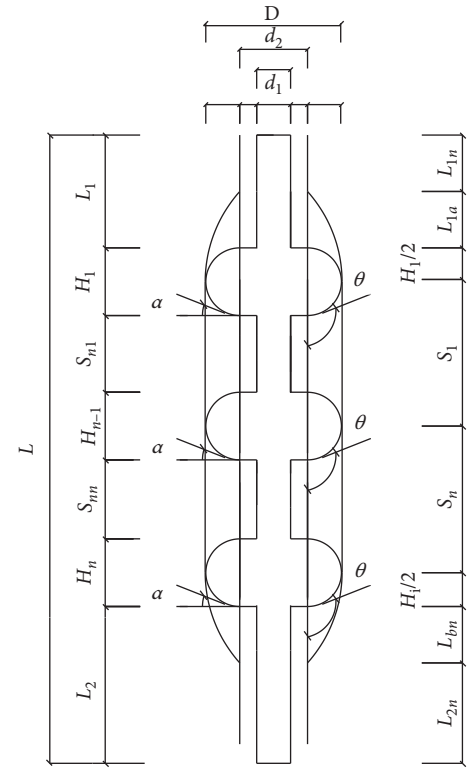

Figure 19: $S_i < 3D$, pile with multiple nodular parts.

F_{lcn}, FE, and F_p^c is the same as that of the pile with single nodular part.

4.3. Calculation of Bearing Capacity of Compressive Pile with Multiple Nodular Parts. Similar to the compressive capacity of the pile with two nodular parts, the failure pattern of the pile will be different according to the distance between the nodular parts. When $S_i \geq 3D$, that is, when the distance between the nodular parts is large, it will show the failure pattern in Figure 18. When $S_i < 3D$, that is, when the distance between the nodular parts is small, the failure pattern in Figure 19 will appear.

4.3.1. When $S_i \geq 3D$, Calculation of Bearing Capacity of Compressive Pile with Multiple Nodular Parts. When $S_i \geq 3D$, the influence between the nodular parts is negligible and the failure pattern of soil around the nodular part is similar to that of the pile with single nodular part. Therefore, the bearing capacity calculation method of the nodular part of the pile with two nodular parts can be regarded as the sum of the bearing capacity of n nodular parts.

$$F_u = F_t + n\left(F_{\mathrm{cn}} + F_{\mathrm{sn}}\right) + F_{\mathrm{sf}}, \quad F_u < F_p^c, \tag{27}$$

where $F_{\mathrm{sf}} = f_s \pi d_2 L_0 = f_s \pi d_2 (L - \sum_{i=1}^{n} H_i - \sum_{i=1}^{n} L_{\mathrm{ai}} + \sum_{i=1}^{n} \gamma_i L_{\mathrm{bi}})$; the calculation formula of F_{cn}, F_{sn}, and F_p^c is the same as that of the pile with single nodular part.

4.3.2. When $S_i < 3D$, Calculation of Bearing Capacity of Compressive Pile with Multiple Nodular Parts. When $S_i < 3D$, the influence between the upper and the lower nodular part is large. The failure pattern of the soil of the upper part of the upper nodular part and the lower part of the lower nodular part is basically similar to that of the pile with single nodular part. The bearing capacity of the nodular part is mainly borne by the curve section and the straight section of the bottom nodular part.

$$F_u = F_t + F_{\mathrm{cn}} + F_{\mathrm{sn}} + F_{\mathrm{sf}} + F_{\mathrm{ln}}, \quad F_u < F_p^c, \tag{28}$$

where $F_{\mathrm{sf}} = f_{\mathrm{lf}} \pi d_1 L_0 = f_s \pi d_1 (L_1 + L_2 - L_{a1} + \gamma_n L_{bn})$; $F_{\mathrm{ln}} = f_s \pi d_1 L_0 = f_s \pi d_1 (\sum_{i=1}^{n} S_i + ((H_1 + H_n)/2))$, and the calculation formula of F_{cn}, F_{sn}, and F_p^c is the same as that of the pile with single nodular part.

In practical engineering, for piles with multiple nodular parts, there may be a situation in which the spacing between two nodular parts is larger, while the spacing between other two nodular parts is smaller. An equal spacing and nodular part diameter can help to maximize the performance of pile with multiple nodular parts; the uniform arrangement of the nodular part is the best in the field application [34, 35]. In the design of squeezed nodular pile, the spacing of the nodular part should be evenly distributed to avoid complicated

calculation. If it is indeed necessary to arrange the nodular part of the pile in an uneven way, the ultimate bearing capacity of the single pile with nonuniformly distributed nodular part should be calculated according to the single pile bearing capacity calculation principle of double nodular part and multiple nodular part.

5. Conclusions

This paper took vortex-compression nodular pile as the research object, and indoor model test and ABAQUS finite element software were used to analyze the compressive capacity and bearing characteristics of nodular piles. The load-settlement relationship, axial force transfer curve of the pile body, displacement, and plastic strain of the soil in and around the pile body were analyzed under the conditions of different number, diameter, and distance of nodular parts. In this paper, the virtual work principle and slip line theory are used to solve the bearing capacity of the curve section of the nodular part. The bearing capacity of the single nodular part, the double nodular part, and the multiple nodular part under the action of the down pressure load is analyzed and deduced. By modifying the traditional pile with nodular diameter formula, the calculation method of compressive bearing capacity of the pile with nodular part is improved, more accord with the actual conditions. A series of formulas in this paper improve the fuzzy part of the traditional empirical formula on the calculation of the nodular pile and improve the theoretical research of the nodular pile. The conclusions are as follows.

The nodular pile has a significantly higher compressive bearing capacity than equal-section pile. For pile with single nodular part, the position of the nodular part greatly influences the bearing capacity of single pile. In the design of monopile, it is better to set the nodular part close to the bottom of pile. For the pile with double nodular parts with the same nodular part spacing, the position of the nodular parts has little effect on the bearing capacity of nodular pile. When fixing the lower nodular part, moving the upper nodular part to higher position increases the bearing capacity of pile, but the spacing of the nodular parts should not exceed 6 times of the height of the nodular parts. For piles with three nodular parts, if the spacing of the nodular parts is reasonable, the bearing capacity of monopile can be regarded as the sum of bearing capacity of a pile with two nodular parts and a pile with single nodular part.

The nodular parts play an important role in the process of load transfer. It can be known that the bearing capacity of the curve section of the nodular part depends on the diameter of the nodular part and the diameter of straight section of the nodular part. It is also influenced by the cohesion coefficient of the soil around the pile and the internal friction angle of the soil around the pile.

The nodular pile will face a complicated working environment in the actual project. In the future, it is necessary to conduct the serial studies on the deformation characteristics and stress mechanism of the nodular pile group and on the mechanical properties of the nodular pile and the soil around the pile under seismic load.

Data Availability

The data used to support the findings of this study are available from the corresponding author upon request.

Conflicts of Interest

The authors declare that they have no conflicts of interest.

Acknowledgments

The authors kindly thank the Research Center of Civil Engineering, China University of Petroleum (East China), for providing finite element software and workstation. This research was funded by the National Natural Science Foundation of China (grant no. 41907239).

References

[1] F. Chen, K. X. Wu, and S. He, "A Field test study on bearing capacity of squeezed branch pile," *Chinese Journal of Geotechnical Engineering*, vol. 35, no. 2, pp. 990–993, 2013.

[2] J. Q. Jiang, "Bearing capacity and mechanical behavior experiment on large diameter-expanding pile," *Advanced Materials Research*, vol. 243–249, no. 492, pp. 457–460, 2011.

[3] M. E. Al-Atroush, A. Hefny, Y. Zaghloul, and T. Sorour, "Behavior of a large diameter bored pile in drained and undrained conditions: comparative analysis," *Geosciences*, vol. 10, no. 7, Article ID 10070261, 2020.

[4] L. Kondratieva, V. Konyushkov, L. V. Trong, and V. Kirillov, "Analysis of bored piles' field test results," *Key Engineering Materials*, vol. 828, pp. 194–201, 2020.

[5] X. F. Zhang, Y. Ma, and C. X. Song, "Research on ultimate friction's depth effect of soil around bored pile," *Applied Mechanics and Materials*, vol. 90–93, pp. 52–55, 2011.

[6] R. Hill, *The Mathematical Theory of Plasticity*, Oxford University Press, Oxford, UK, 1950.

[7] G. T. Houlsby and H. S. Yu, "Finite cavity expansion in dilatant soils: loading analysis," *Géotechnique*, vol. 41, no. 2, pp. 173–183, 1991.

[8] J. Y. Cui, *Experimental Study on Bearing Mechanism and Bearing Capacity of Cast in Place Pile with Branches and Plates*, Northern Jiaotong University Press, Beijing, China, 1996.

[9] J. Hu, H. Zhang, and H. S. Chen, "Research on the mechanism and calculation formula of bearing capacity improvement," *Anhui Architecture*, vol. 12, no. 3, pp. 58–107, 2005.

[10] M. Zhou, Z. F. Wang, and S. W. Wang, "Non-linear finite element analysis of squeezed branch pile," *Advanced Materials Research*, vol. 243–249, pp. 2409–2414, 2011.

[11] X. Ye, S. Wang, S. Zhang, X. Xiao, and F. Xu, "The compaction effect on the performance of a compaction-grouted soil nail in sand," *Acta Geotechnica*, vol. 15, no. 10, pp. 2983–2995, 2020.

[12] C.-W. Lee, Y.-S. Kim, and S.-Y. Park, "Development of prebored screw pile method and evaluation of its bearing characteristics," *Marine Georesources & Geotechnology*, vol. 34, no. 1, pp. 42–56, 2016.

[13] W. Cui and Z. J. Wang, "Field experiment study on the bearing characteristics of squeezed branch pile in loess area," *Applied Mechanics and Materials*, vol. 166–169, pp. 1329–1332, 2012.

[14] Q. G. Yang, Y. H. Chen, J. Tian, and J. Liu, "Model test research on horizontal bearing characteristics of close-ended

valibale section pipe pile," *Applied Mechanics and Materials*, vol. 638–640, pp. 475–479, 2014.

[15] Z. B. Wang, J. C. Liu, C. Gu, and C. Z. Sun, "Model test study on vertical static bearing behaviors of DX pile with stepped variable cross-section," *Science Technology and Engineering*, vol. 18, no. 14, pp. 67–72, 2018.

[16] K. N. Zhang and J. Liu, "Analysis of pile load-transfer under pile-side softening," *Journal of Central South University of Technology*, vol. 10, no. 3, pp. 231–236, 2003.

[17] J.-j. Zhou, K.-h. Wang, X.-n. Gong, and R.-h. Zhang, "Bearing capacity and load transfer mechanism of a static drill rooted nodular pile in soft soil areas," *Journal of Zhejiang University Science A*, vol. 14, no. 10, pp. 705–719, 2013.

[18] B. EI-Garhy, A. A. Galil, A. F. Youssef, and M. A. Raia, "Behavior of raft on settlement reducing piles: experimental model study," *Journal of Rock Mechanics and Geotechnical Engineering*, vol. 5, no. 5, pp. 389–399, 2013.

[19] G. Abate, S. Grasso, and M. R. Massimino, "The role of shear wave velocity and non-linearity of soil in the seismic response of a coupled tunnel-soil-above ground building system," *Geosciences*, vol. 9, no. 11, p. 473, 2019.

[20] D. Zhang, F. Luo, Z. Zhu et al., "A constitutive model for saturated gravelly sand based on higher-order dilatancy equation," *Advances in Civil Engineering*, vol. 2020, Article ID 4509057, 18 pages, 2020.

[21] N. N. S. Yapage and D. S. Liyanapathirana, "Implementation of an elasto-plastic constitutive model for cement stabilized clay in a non-linear finite element analysis," *Engineering Computations*, vol. 30, no. 1, pp. 74–96, 2013.

[22] N. Terfaya, A. Berga, M. Raous, and N. Abou-Bekr, "A contact model coupling friction and adhesion: application to pile/soil interface," *International Review of Civil Engineering (IRECE)*, vol. 9, no. 1, pp. 20–30, 2018.

[23] V. N. Quoc, F. Behzad, and H. Aslan, "Influence of size and load-bearing mechanism of piles on seismic performance of buildings considering soil–pile–structure interaction," *International Journal of Geomechanics*, vol. 17, no. 7, Article ID 0000869, 2017.

[24] S. H. Lee, A. Abolmaali, K. J. Shin, and H. D. Lee, "ABAQUS modeling for post-tensioned reinforced concrete beams," *Journal of Building Engineering*, vol. 30, Article ID 101273, 2020.

[25] A. P. Dyson and A. Tolooiyan, "Optimisation of strength reduction finite element method codes for slope stability analysis," *Innovative Infrastructure Solutions*, vol. 3, no. 1, pp. 1–12, 2018.

[26] M. F. Alwalan and M. H. EI Naggar, "Finite element analysis of helical piles subjected to axial impact loading," *Computers and Geotechnics*, vol. 123, Article ID 103597, 2020.

[27] H. C. Yeo, J. Hong, M. Lakshmanan, and D.-Y. Lee, "Enzyme capacity-based genome scale modelling of CHO cells," *Metabolic Engineering*, vol. 60, pp. 138–147, 2020.

[28] Z. X. Yang, Y. Y. Gao, R. J. Jardine, W. B. Guo, and D. Wang, "Large deformation finite-element simulation of displacement-pile installation experiments in sand," *Journal of Geotechnical and Geoenvironmental Engineering*, vol. 146, no. 6, Article ID 0002271, 2020.

[29] P. Alimohammadi, K. A. Kassim, and R. Nazir, "Behaviour of expanded piles under upward loading due to radial preloading in soft clay," *Arabian Journal of Geoences*, vol. 9, no. 2, pp. 1–12, 2016.

[30] S. Z. Cheng, F. Y. Zhang, R. Cong, and L. L. Liu, "Numerical simulation analysis of the effective length about single pile," *Applied Mechanics and Materials*, vol. 501–504, pp. 75–78, 2014.

[31] D. Sheng, S. Zhang, and Z. Yu, "Unanswered questions in unsaturated soil mechanics," *Science China Technological Sciences*, vol. 56, no. 5, pp. 1257–1272, 2013.

[32] R. Ziaie-Moay, M. Kamalzare, and M. Safavian, "Evaluation of piled raft foundations behavior with different dimensions of piles," *Journal of Applied Sciences*, vol. 10, no. 13, pp. 1320–1325, 2010.

[33] P. P. Ni, S. Mangalathu, L. H. Song, G. X. Mei, and Y. L. Zhao, "Displacement-dependent lateral earth pressure models," *Journal of Engineering Mechanics*, vol. 144, no. 6, Article ID 0001451, 2018.

[34] X. Y. Ye, S. Y. Wang, X. Xiao et al., "Numerical study for compaction-grouted soil nails with multiple grout bulbs," *International Journal of Geomechanics*, vol. 19, no. 2, 2019.

[35] X. Y. Ye, S. Y. Wang, Q. Li et al., "Negative effect of installation on performance of a compaction-grouted soil nail in poorly graded stockton beach sand," *Journal of Geotechnical and Geoenvironmental Engineering*, vol. 146, no. 8, 2020.